MODEL-BASED IMAGE RECONSTRUCTION OF CHEMILUMINESCENCE USING A PLENOPTIC 2.0 CAMERA

Hung Nien, Jeffrey A. Fessler

EECS Department
University of Michigan, Ann Arbor

Volker Sick

ME Department
University of Michigan, Ann Arbor

ABSTRACT

Resolving the 3-D structure of translucent objects is of fundamental interest in combustion research. Recent progress in light-field imaging systems provides a single-shot, single-access-point imaging tool for volumetric image reconstruction. However, when a translucent object being imaged has low contrast edges, the conventional block-matching depth reconstruction algorithm used in commercial plenoptic cameras performs poorly. To solve this problem, this paper investigates reconstructing translucent objects using a model-based image reconstruction (MBIR) method. Preliminary simulation results illustrate that useful 3D object information can be resolved using MBIR methods. However, severe z-direction dispersion is observed in the reconstructed images due to the limited angular variation of incident light rays.

1. INTRODUCTION

Resolving the instantaneous 3-D structure of translucent objects such as mixing fuel sprays and flame fronts is of considerable interest and has motivated various 3-D imaging techniques. Early work on laser-sheet-based 3-D imaging used phase-locked or time-averaged measurements and stacks of images that were then rendered to yield averaged volumetric data. Instantaneous measurements for scalar quantities emerged, including techniques that simultaneously used multiple light sheets, a moving light sheet, and tomographic methods. For velocity measurements, tomographic particle image velocimetry (Tomo-PIV) [1] has been used with 4-6 cameras having independent fields of view and offers excellent 3-D reconstruction of the flow field. However, demands on calibration among cameras and optical access restrain the practical application of Tomo-PIV. For example, technical combustion applications, such as high-pressure gas turbine combustors or internal combustion engines, substantially limit optical access. Therefore, 3-D measurement techniques

that need less optical access are important for combustion research.

The emerging imaging technology using light-field imaging systems such as the Lytro [2] and Raytrix [3] plenoptic cameras provides single-shot, single-access-point imaging tools for instantaneous volumetric imaging. Such systems can estimate 3-D flame chemiluminescence [4] and have been applied to PIV [5]. However, even when using a simplified (plenoptic 1.0) system model, the existing plenoptic-camera-based PIV method [5] involved precomputing and storing an enormous system matrix, making it computational intensive. This paper considers a more realistic (plenoptic 2.0) system model for sensors having lenslet arrays with multiple focal distances [6], and proposes a practical approximation for efficient on-the-fly computation. Furthermore, instead of simply matching the forward model with the possibly inconsistent measurements (due to noise and model mismatch), we reconstruct images using a model-based image reconstruction (MBIR) method [7], in which one models the physics of the imaging system, the statistics of the measurements, the prior information about the object being imaged, and then finds the best fitting object estimate by an iterative algorithm that minimizes a cost function related to those models.

## 2. IMAGING MODEL AND RECONSTRUCTION

A (lenslet-based) plenoptic camera consists of three parts: the main lens, the micro-lens array, and image sensors. Unlike conventional cameras, light rays entering a plenoptic camera are re-directed by a set of micro-lenses (i.e., micro-lens array) in the camera and then recorded by image sensors placed behind the micro-lens array, generating unconventional image data with embedded angular information of light rays.

Fig. 1 shows a 2-D schematic of a plenoptic camera. For a point source p located at distance z from the main lens, the main lens first forms a virtual object p' in the camera, positioned at the distance z' from the main lens, where, by the thin-lens formula:

$$\frac{1}{z} + \frac{1}{z'} = \frac{1}{F}, \tag{1}$$

where F denotes the focal distance of the main lens. The virtual object p' can be either in front of the micro-lens array
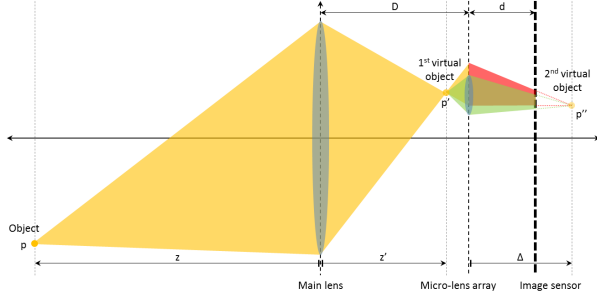
Fig. 1. 2-D schematic of a plenoptic camera.

($z' < D$) or behind the micro-lens array ($z' > D$). The ith micro-lens, with focal distance f_i, then forms a second virtual object p_i'' at a distance Δ from the micro-lens array, casting an image of p' on the image sensors located at the distance d from the micro-lens array. The captured image data of p, i.e., the point spread function (PSF) of the unit point source p, is the superposition of all micro-lens images.

Let $h(\underline{u}; \underline{x})$ denote the PSF of a unit point source located at $\underline{x} = (x, y, z)$, where $\underline{u} = (u, v)$ is the image sensor coordinates. The overall PSF is given by

$$h(\underline{u}; \underline{x}) = \sum_i h_i(\underline{u}; \underline{x}) \,, \tag{2}$$

where h_i denotes the ith micro-lens PSF image. When the main lens and all micro-lenses have round apertures, h_i is a product of two (not necessarily aligned) disk functions, i.e., the image of p' assuming open micro-lens aperture (the red cone in Fig. 1) and maximum support of the image of p' assuming open main lens aperture (the green cone in Fig. 1) [6].

To derive the discrete PSF, we simply parameterize both the captured image and the object to be imaged with some basis functions (2-D rectangular function for square pixels and 3-D rectangular function for cubic voxels in our experiments), and the discrete PSF can be represented as

$$h[\underline{k}; \underline{l}] \triangleq \int \left(\int h(\underline{u}; \underline{x}) \, \beta_1(\underline{l}; \underline{x}) \, \mathrm{d}\underline{x} \right) \beta_2(\underline{k}; \underline{u}) \, \mathrm{d}\underline{u} \,, \tag{3}$$

where $\underline{k} = (k_u, k_v)$, $\underline{l} = (l_x, l_y, l_z)$, and β_1 and β_2 denote the voxel and pixel basis functions, respectively. For a translucent object $p[\underline{l}]$, the image $q[\underline{k}]$ captured by the plenoptic camera can be expressed as

$$q[\underline{k}] = \sum_{\underline{l}} h[\underline{k}; \underline{l}] \, p[\underline{l}] \,. \tag{4}$$

A more compact matrix-vector multiplication form is

$$\mathbf{y} = \mathbf{A}\mathbf{x} \,, \tag{5}$$

where $\mathbf{y}$ and $\mathbf{x}$ stack the entries of $q[\underline{k}]$ and $p[\underline{l}]$ into vectors, and $\mathbf{A}$ is a matrix rearrangement of $h[\underline{k}; \underline{l}]$.

2.1. Approximation of the system matrix

Although we have the closed-form expression (3) for each element of $\mathbf{A}$, computing of $\mathbf{A}$ is non-trivial. Due to the re-direction of micro-lenses, $h[\underline{k}; \underline{l}]$ is highly shift-variant, and $\mathbf{A}$ is non-structured. Thus, one must precompute (or compute on-the-fly) elements of the enormous (but sparse) $\mathbf{A}$. Furthermore, being a product of two disk functions, h_i is non-separable. This makes (3) non-separable, even with separable and shift-invariant β_1 and β_2, leading to a time-consuming 5-D numerical integration for each element of $\mathbf{A}$.

To reduce computation of $\mathbf{A}$, we observed that for typical experimental setups ($f_i \approx d$, and z is large enough),

$$\iint h(\underline{u}; \underline{x}) \, \beta_1(\underline{l}; \underline{x}) \, \mathrm{d}x \mathrm{d}y \tag{6}$$

is approximately the product of a sharp disk function and a z-dependent blurred disk function that we precompute and tabulate. Thus, one can avoid 2-D integration over x and y by applying this approximation when computing elements of $\mathbf{A}$.

2.2. Tomographic image reconstruction

Having defined the system matrix $\mathbf{A}$, we reconstruct the object being imaged $\mathbf{x}$ from the captured image data $\mathbf{y}$ by solving the following regularized least-squares problem with a non-negativity constraint:

$$\hat{\mathbf{x}} \in \arg\min_{\mathbf{x} \succeq \mathbf{0}} \left\{ \tfrac{1}{2} \|\mathbf{y} - \mathbf{A}\mathbf{x}\|_2^2 + \mathsf{R}(\mathbf{x}) \right\} \,, \tag{7}$$

where R denotes an edge-preserving regularizer that penalizes the roughness of the reconstructed image $\mathbf{x}$.

In our simulation experiments, we used a "corner-rounded" anisotropic total-variation (TV) regularizer R that encourages $\mathbf{x}$ to be piece-wise smooth. To solve the minimization problem (7), we used the fast iterative shrinkage/thresholding algorithm (FISTA) [8]:

$$\begin{cases} \mathbf{x}_{k+1} = \left[\mathbf{z}_k - \tfrac{1}{L} \left(\mathbf{A}' \left(\mathbf{A}\mathbf{z}_k - \mathbf{y} \right) + \nabla\mathsf{R}(\mathbf{z}_k) \right) \right]_+ \\ \theta_{k+1} = \left(1 + \sqrt{1 + 4\theta_k^2} \right)/2 \\ \mathbf{z}_{k+1} = \mathbf{x}_{k+1} + \tfrac{\theta_k - 1}{\theta_{k+1}} \left(\mathbf{x}_{k+1} - \mathbf{x}_k \right) \,, \end{cases} \tag{8}$$

where L is the maximum eigenvalue of $\mathbf{A}'\mathbf{A}$, $\mathbf{z}_0 = \mathbf{x}_0$ is the zero initial image, $\theta_0 = 1$, and $[\cdot]_+$ denotes the operator that clips all negative values of the input vector. For faster convergence, we applied an adaptive restart scheme [9].

3. SIMULATION EXPERIMENTS

To illustrate the feasibility of translucent object reconstruction by solving (7), we performed some preliminary simulations of 3-D image reconstruction using a plenoptic camera. Fig. 2 shows the setup of our numerical simulation. A $50 \times 50 \times 50$ [mm^3] image volume is placed at 700 [mm]
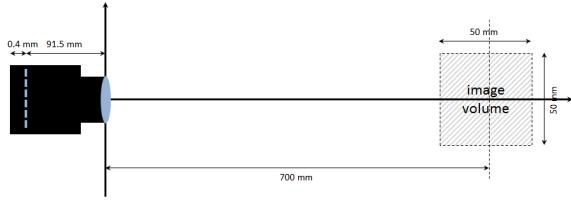
**Fig. 2**. Setup of the numerical simulation.
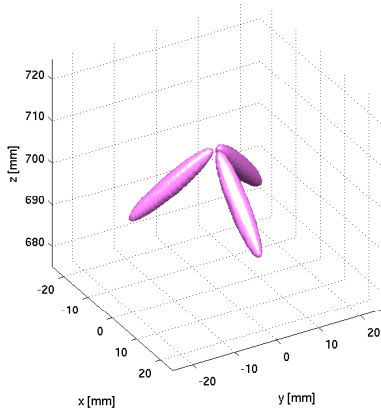
Fig. 3. Torch phantom used in the simulation.

in front of our simulated plenoptic camera, where the main lens radius is 31.02 [mm] with focal length $F = 0.35$ [mm], the distance between the main lens and the micro-lens array is $D = 91.5$ [mm], and the distance between the micro-lens array and the image sensor is $d = 0.4$ [mm]. Our simulation used a hexagonal micro-lens array where each micro-lens has radius 0.135 [mm] and focal length $f_i = 0.35$ [mm]. For efficient simulation, the image size of the simulated plenoptic camera is 850×850, and we discretized the image volume into $100 \times 100 \times 100$ isotropic cubic voxels.

Fig. 3 illustrates a torch phantom consisting of three ellipsoids with uniform intensity 10. The angle between each ellipsoid and the optical path is $45°$. Fig. 4 shows the image captured by the simulated plenoptic camera with additive Gaussian noise (standard deviation 0.1), where the peak value of the noiseless image is about 2.15. To avoid an "inverse crime," we generated the simulated image using a high-resolution torch phantom with finer voxel sizes ($0.5\times$ in each dimension). We ran 500 iterations of (8) to reconstruct the torch phantom. The system matrix $\mathbf{A}$ was precomputed and stored in memory as a sparse matrix. Since we used the PSF approximation mentioned in Section 2.1, we expected greater model mismatch in the transaxial plane. Hence, we regularize the image roughness more transaxially.

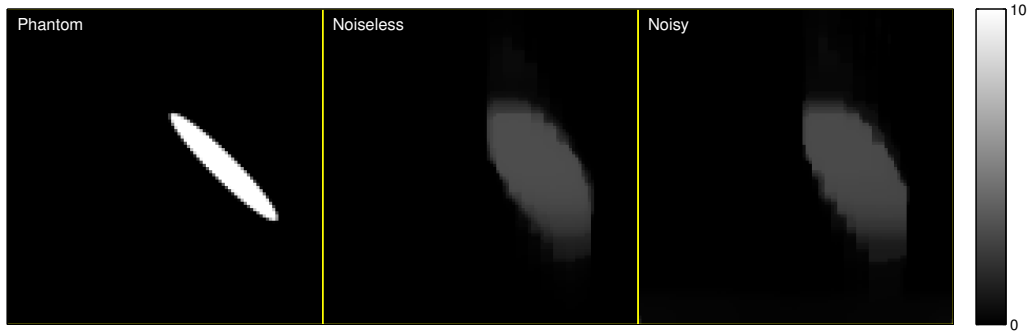Fig. 5 shows the reconstructed images (with isosurface
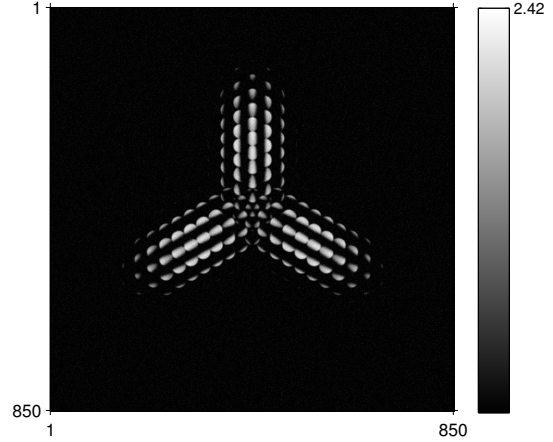
Fig. 4. The image captured by the simulated plenoptic camera in the noisy condition.
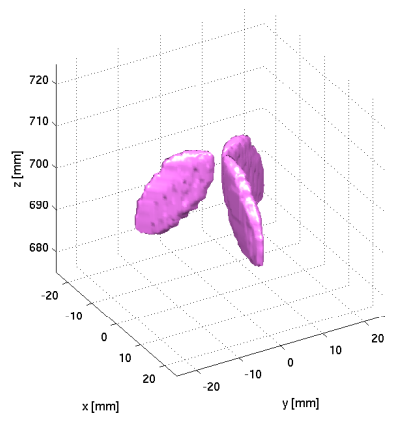
threshold 2) for noiseless and noisy conditions. The reconstructed images recovered the geometry (e.g., the angular information) of the phantom but showed strong dispersion in the z-direction. To illustrate the effect of dispersion, Fig. 6 shows $x - z$ slices of the phantom and reconstructed images at $y \approx 0$ [mm]. The reconstructed images have much smaller intensity than the phantom. Fig. 7 shows the projections of the image slices shown in Fig. 6. These projections match very well (the non-zero bias in the noisy reconstruction might come from the non-zero mean of non-negative clipped noise), implying that the reconstructed images are dispersed in the z-direction. Finally, due to the z-dependent dispersion, the angles between the reconstructed lobes and the optical path appear somewhat smaller than $45°$. In fact, due to the limited angular variation of incident light rays, the reconstructed images have poor depth resolution, as in digital tomosynthesis imaging [10–12].

4. CONCLUSIONS

This paper considered resolving the 3-D structure of translucent objects from image data captured by a lenslet-based plenoptic camera using a model-based image reconstruction method. Preliminary simulation results showed that one can roughly resolve the 3-D structure of an object being imaged; however, the reconstructed image suffers from severe dispersion in the z-direction. To overcome this problem, we can either use anisotropic cubic voxels (longer in the z-direction) or encourage some form of sparsity of the reconstructed image, leading to a more sophisticated cost function with a non-smooth regularization term. As future work, we will study the above modifications, investigate using a micro-lens array with multiple focal distances, and reconstruct image volumes from real plenoptic camera data.

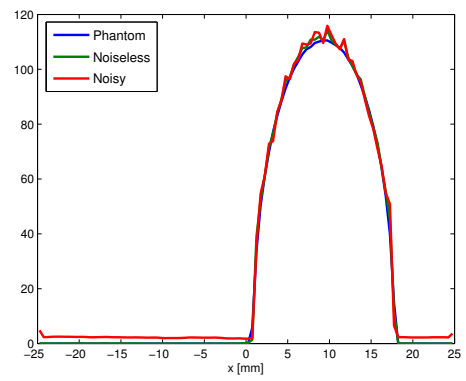Fig. 6. Slices of the phantom and reconstructed images at $y \approx 0$ [mm].

(a)
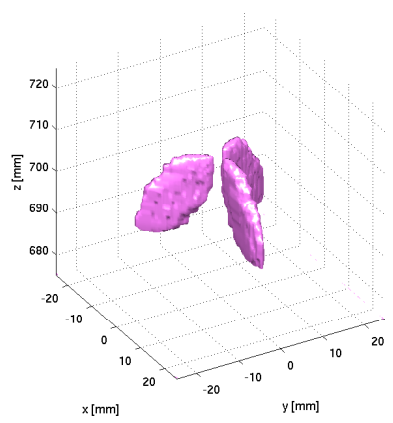
(b)

Fig. 5. The reconstructed images (with isosurface threshold 2) in the (a) noiseless and (b) noisy conditions.

Fig. 7. Projections of the image slices showing in Fig. 6.

5. REFERENCES

[1] G. E. Elsinga, F. Scarano, B. Wieneke, and B. W. Van Oudheusden, "Tomographic particle image velocimetry," *Experiments in Fluids*, vol. 41, no. 6, pp. 933–47, 2006.

[2] R. Ng, M. Levoy, M. Brédif, G. Duval, M. Horowitz, and P. Hanrahan, "Light field photography with a hand-held plenoptic camera," 2005, Stanford Tech Report CTSR 2005-02.

[3] C. Perwass and L. Wietzke, "Single lens 3d-camera with extended depth-of-field," in *Proc. SPIE 8291 Human Vision and Electronic Imaging XVII*, 2012, p. 829108.

[4] M. L. Greene and Volker Sick, "Volume-resolved flame chemiluminescence and laser-induced fluorescence imaging," *Applied Physics B*, vol. 113, no. 1, pp. 87–92, 2013.

[5] T. W. Fahringer and B. S. Thurow, "Tomographic reconstruction of a 3-D flow field using a plenoptic camera," in *Proc. 42nd AIAA Fluid Dynamics Conf. and Exhibit*, 2012.

[6] T. E. Bishop and P. Favaro, "The light field camera: extended depth of field, aliasing, and superresolution," *IEEE Trans. Patt. Anal. Mach. Int.*, vol. 34, no. 5, pp. 972–86, May 2012.

[7] J. Nuyts, B. De Man, J. A. Fessler, W. Zbijewski, and F. J. Beekman, "Modelling the physics in iterative reconstruction for transmission computed tomography," *Phys. Med. Biol.*, vol. 58, no. 12, pp. R63–96, June 2013.

[8] A. Beck and M. Teboulle, "A fast iterative shrinkage-thresholding algorithm for linear inverse problems," *SIAM J. Imaging Sci.*, vol. 2, no. 1, pp. 183–202, 2009.

[9] B. O'Donoghue and E. Candès, "Adaptive restart for accelerated gradient schemes," *Found. Comput. Math.*, vol. 13, July 2013.

[10] D. G. Grant, "Tomosynthesis: a three-dimensional radiographic imaging technique," *IEEE Trans. Biomed. Engin.*, vol. 19, no. 1, pp. 20–8, Jan. 1972.

[11] J. T. Dobbins and D. J. Godfrey, "Digital x-ray tomosynthesis: current state of the art and clinical potential," *Phys. Med. Biol.*, vol. 48, no. 19, pp. R65–106, Oct. 2003.

[12] I. Sechopoulos, "A review of breast tomosynthesis. Part II. Image reconstruction, processing and analysis, and advanced applications," *Med. Phys.*, vol. 40, no. 1, pp. 014302, Jan. 2013.